

Supplementary Information for

Heteroleptic diradical Cr(III) complex with extended spin delocalization and large intramolecular magnetic exchange

Xiaozhou Ma,^a Elizaveta A. Suturina,^b Mathieu Rouzières,^a Fabrice Wilhelm,^c
Andrei Rogalev,^c Rodolphe Clérac,^{*a} Pierre Dechambenoit^{*a}

^a *Univ. Bordeaux, CNRS, Centre de Recherche Paul Pascal, CRPP, UMR 5031, 33600 Pessac, France.*

^b *Centre for Sustainable Chemical Technologies (CSCT), University of Bath, Claverton Down, Bath BA2 7AY, UK.*

^c *ESRF-The European Synchrotron, 38043 Grenoble Cedex 9, France.*

Emails: rodolphe.clerac@crpp.cnrs.fr; pierre.dechambenoit@crpp.cnrs.fr

Table of Contents

1. Experimental and synthetic methods	S3
a. Experimental techniques	S3
b. Syntheses	S5
2. Crystallographic Studies	S6
Figure S1. ORTEP-type views of the Cr(tpy)(CF ₃ SO ₃) ₃ complex	S6
Figure S2. ORTEP-type views of the cationic complexes in 1 , 1^{red} and 1^{redred}	S6
Table S1. Crystal data and structure refinements	S7
3. Spectroscopy data	S8
Figure S3. X-ray absorption spectroscopy (XAS) at Cr K-edge region for 1 and 1^{red}	S8
Figure S4. UV/visible/NIR spectra of 1 , 1^{red} and 1^{redred} in CH ₃ CN	S9
4. Electrochemistry	S10
Figure S5. Cyclic voltammograms in CH ₃ CN at different scan rates	S10
5. Computational details: DFT and CASSCF studies	S11
a. Ab initio ligand field analysis	S11
Figure S6. Ligand field splitting for the Cr(III) sites	S11
b. Exchange interaction from broken-symmetry approach	S12
Table S2. Computed local spin Hamiltonian parameters	S12
Figure S7. SOMOs of [Cr(tphz)(tpy)] ³⁺ in 1	S13
Figure S8. SOMOs of [Cr ^{III} (tphz ⁺)(tpy)] ²⁺ in 1^{red}	S13
Table S3. Computed energies and corresponding S ² expectation values for 1^{redred}	S13
Figure S9. SOMOs of [Cr ^{III} (tphz ⁺)(tpy ⁻)] ⁺ in 1^{redred}	S14
6. Additional magnetic data	S15
Figure S10. Temperature dependence of the χT product & M vs. HT^{-1} data for 1	S15
Figure S11. Temperature dependence of the χT product & M vs. HT^{-1} data for 1^{red}	S16
Figure S12. Temperature dependence of the χT product & M vs. H data for 1^{redred}	S17
7. References	S19

1. Experimental and synthetic methods

a. Experimental technics

Elemental analyses (EA) were performed on a ThermoFischer Flash EA 1112.

FT-IR spectra were recorded at room temperature on a Thermal Scientific Nicolet™ 6700 ATR (attenuated total reflection) spectrometer equipped with a Smart iTR diamond window.

UV-vis-NIR spectra were recorded using a Perkin Elmer LAMBDA 950 in dry acetonitrile.

Crystallographic data were collected with a Bruker APEX II Quasar diffractometer, equipped with a graphite monochromator centred on the path of MoK α radiation ($\lambda = 0.71073 \text{ \AA}$). The single crystals were coated with Cargille™ NHV immersion oil and mounted on a fiber loop, followed by data collection at 120 K. The program SAINT was used to integrate the data, which was thereafter corrected using SADABS.^[1] The structures were solved using direct methods and refined by a full-matrix least-squares method on F^2 using SHELXL-2014.^[2] All non-hydrogen atoms were refined with anisotropic displacement parameters. Hydrogen atoms were assigned to ideal positions and refined isotropically using a riding model.

For **Cr(tpy)(O₃SCF₃)₃**, the asymmetric unit contains two different complexes, which differ slightly by the orientation of the triflate anions. Another smaller unit cell was considered with only one complex in the asymmetric unit, but the resolution give rise to a disorder on one of the equatorially coordinated triflate.

For **1**, the diffraction data were cut at 0.90 Å as no diffraction was observed above this limit. The crystal structure contains one diethyl ether solvent molecule which was found to be highly disordered. This lattice solvent molecule was modeled using SADI, DFIX and SIMU constraints/restraints. Two triflate anions were also found to be also disordered and were refined using the same restraints.

For **1^{red}**, all the tested crystals were very small and weakly diffracting so that the diffraction data were cut at 1.00 Å. The result is a quite low θ_{max} value as well as poor resolution and data/parameters ratio.

For **1^{redred}**, one of the acetonitrile molecules was found to be disordered over two positions and resides on an inversion centre, the two positions being therefore equivalent by symmetry. N11 and C48 atoms reside on the same position and were refined using EADP and EXYZ constraints. C47A and C47B atom positions were constrained at fixed positions as these atoms are very close to an inversion centre at 0.5 0.5 0. The hydrogens on the disordered acetonitrile (on C48) were not introduced but were taken into account in the compound formula.

The crystallographic data are listed in Table S1. The CIF files have been deposited at the Cambridge Crystallographic Data Centre as supplementary publication no. CCDC 1954799-1954802.

Electrochemistry: Cyclic voltammetry (CV) measurements were performed with a Metrohm Autolab PGSTAT101 equipped with a platinum working electrode. Ferrocene was used as an internal reference. Measurements were done in CH₃CN with 0.1 M (*n*-Bu₄N)PF₆ as supporting electrolyte and at scan rates ranging from 0.01 to 0.2 V/s.

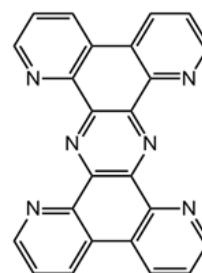
X-ray absorption spectroscopy. XAS spectra (Figure S3) were obtained at the ID12 beamline (ESRF – The European Synchrotron) on pressed pellets of polycrystalline samples of **1** and **1^{red}**. We used fundamental harmonic of Apple-II type undulator for experiments at the Cr K-edge. The XAS spectra were recorded using total fluorescence yield detection mode and were subsequently corrected for reabsorption effects.

Magnetic susceptibility measurements were performed on a Quantum Design SQUID magnetometer MPMS-XL and PPMS-9 Quantum Design susceptometer at temperatures between 1.8 and 400 K and dc magnetic fields ranging from -7 to 7 T. Measurements were performed on a crystalline powder sample of **1**, **1^{red}** and **1^{redred}** (4.12 & 16.06 mg, 4.3 & 10.0 mg, 12.4 & 5.6 mg respectively) sealed in a polypropylene bag (3 x 0.5 x 0.2 cm: 16.57 & 22.06 mg for **1**, 37.8 & 29.8 mg for **1^{red}**, 36.4 & 39.7 mg for **1^{redred}**). No out-of-phase ac signal was detected in our experimental window above 1.8 K. Prior to the experiments, the field dependent magnetization was measured at 100 K in order to detect the presence of any bulk ferromagnetic impurities. The samples appeared to be free of any significant ferromagnetic impurities. The magnetic data were corrected for the sample holder and the intrinsic diamagnetic contributions.

DFT and CASSCF calculations have been carried out using ORCA 4.1 program^[3] package on the crystal structure of the complexes. Exchange couplings were estimated using the energies and wavefunctions obtained with B3LYP functional and def2-TZVP basis set for various spin states. Ab initio ligand field calculations^[4] have been done with CASSCF(3,5)/def2-TZVP. Spin-Hamiltonian parameters, *D* and *g*, have been computed using the mean field spin-orbit coupling approximation.^[5] Spin density contour plots were visualized using Avogadro version 1.2.0.^[6]

b. Syntheses

$\text{Cr}(\text{tpy})\text{Cl}_3$,^[7] $\text{Cr}(\text{tpy})(\text{O}_3\text{SCF}_3)_3$ ^[8] and tetrapyridophenazine (tphz; Scheme S1)^[9,10,11] were prepared using procedures described in the literature. The exact nature $\text{Cr}(\text{tpy})(\text{O}_3\text{SCF}_3)_3$ was further checked by single-crystal X-ray diffraction and reported here (Figure S1, Table S1). Reactions for the syntheses of complexes **1^{red}** and **1^{redred}** were carried out under a dry nitrogen atmosphere using a glovebox under dinitrogen. Diethyl ether (Et_2O), acetonitrile (CH_3CN) and tetrahydrofuran (THF) were purified using an Innovative Technologies solvent purification system.



Scheme S1. Structure of tphz.

Synthesis of $[\text{Cr}(\text{tphz})(\text{tpy})](\text{CF}_3\text{SO}_3)_3 \cdot \text{Et}_2\text{O}$ (1**).** 20 mg of tphz ligand (0.052 mmol, 1 eq.) were suspended in 10 mL of CHCl_3 at 70°C . A solution of $[\text{Cr}(\text{tpy})(\text{SO}_3\text{CF}_3)_3]$ (76.2 mg, 0.104 mmol, 2 eq.) in acetonitrile (5 mL) was added and the mixture was stirred for 15 hours. The solution was filtered with a sartorius filter. The precipitate was dried under vacuum and dissolved in CH_3CN , and orange needle-shape crystals came out from diethyl ether diffusion into the solution. Yield: 15 mg, 12% based on Cr. Elemental analysis found (calcd) for $\text{C}_{46}\text{H}_{33}\text{CrF}_9\text{N}_9\text{O}_{10}\text{S}_3$: C 44.42(46.39), H 2.23(2.79), N 10.43(10.58), S 7.91(8.08). IR (solid, $\bar{\nu}/\text{cm}^{-1}$) 526 (s), 533 (s), 538 (s), 545 (w), 556 (m), 574 (m), 589 (m), 634 (vs), 660 (m), 704 (w), 712 (w), 775 (m), 804 (m), 1027 (vs), 1150 (s), 1223 (s), 1247 (vs), 1384 (m), 1403 (w), 1451 (m), 1481 (m), 1516 (w), 1606 (m), 1988 (w), 3075(w), 3344 (w).

Synthesis of $[\text{Cr}(\text{tphz})(\text{tpy})](\text{CF}_3\text{SO}_3)_2 \cdot \text{CH}_3\text{CN}$ (1^{red}**).** 9.5 mg of $\text{Cr}(\text{tpy})(\text{SO}_3\text{CF}_3)_3$ (0.013 mmol, 1 eq.), 2.7 mg of cobaltocene (0.014 mmol, 1.1 eq.) and 5 mg of tphz (0.013 mmol, 1 eq.) were reacted in 2 mL CH_3CN at 70°C for 15 hours. The resulting brown solution was filtered through plastic VWR filter (porosity 0.2 μm). Brown needle-shape crystals suitable for X-ray diffraction were obtained from slow diffusion of diethyl ether. Yield: 4 mg, 30% based on Cr. IR (solid, $\bar{\nu}/\text{cm}^{-1}$) 659 (m), 673 (m), 702 (m), 714 (m), 733 (m), 763 (s), 777 (vs), 830 (m), 1000 (s), 1027 (vs), 1147 (vs), 1197 (m), 1223 (s), 1253 (vs), 1350 (w), 1388 (w), 1447 (m), 1475 (m), 1507 (w), 1522 (w), 1580 (w), 1601 (m), 1978 (w), 2252 (w), 3082 (w), 3634 (w).

Synthesis of $[\text{Cr}(\text{tphz})(\text{tpy})]_2(\text{CF}_3\text{SO}_3)_2 \cdot 3\text{CH}_3\text{CN} \cdot 2\text{Et}_2\text{O}$ (1^{redred}**).** 9.5 mg of $\text{Cr}(\text{tpy})(\text{SO}_3\text{CF}_3)_2$ (0.013 mmol, 1 eq.), 5 mg of tphz (0.013 mmol, 1 eq.) and 5.2 mg of cobaltocene (0.027 mmol, 2.1 eq.) were reacted in 2 mL of CH_3CN at 70°C for 15 hours. The resulting brown solution was filtered through plastic VWR filter (porosity 0.2 μm). Black plate-shape crystals suitable for X-ray diffraction were obtained from slow diffusion of diethyl ether. Yield: 5 mg, 41% based on Cr. IR (solid, $\bar{\nu}/\text{cm}^{-1}$) 664 (m), 670 (m), 713 (s), 763 (vs), 827 (m), 930 (s), 997 (s), 1027 (vs), 1078 (s), 1116 (vs), 1145 (vs), 1222 (vs), 1256 (vs), 1348 (m), 1387 (m), 1448 (m), 1502 (w), 1578 (m), 1601 (m), 2199 (w), 3073 (w).

2. Crystallographic Studies

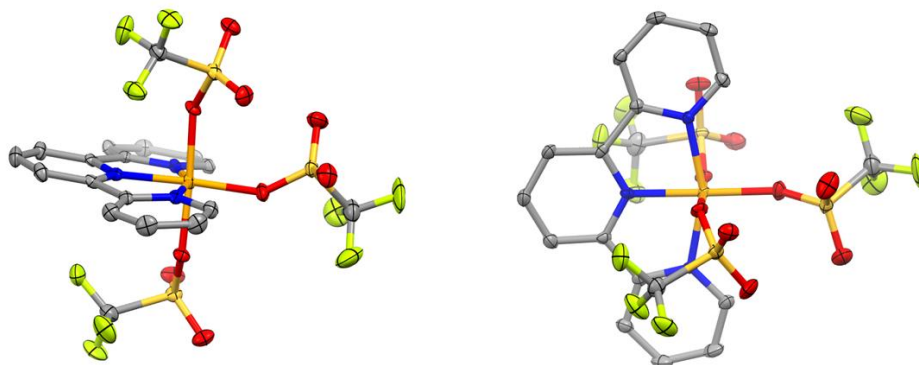


Figure S1. Two perpendicular ORTEP-type views of one of the two $\text{Cr}(\text{tpy})(\text{CF}_3\text{SO}_3)_3$ complex in the asymmetric unit at 120 K. Grey: C; orange: Cr; blue: N; yellow: S; red: O; green: F. Thermal ellipsoids are depicted at a 50 % probability level. H atoms are omitted for clarity.

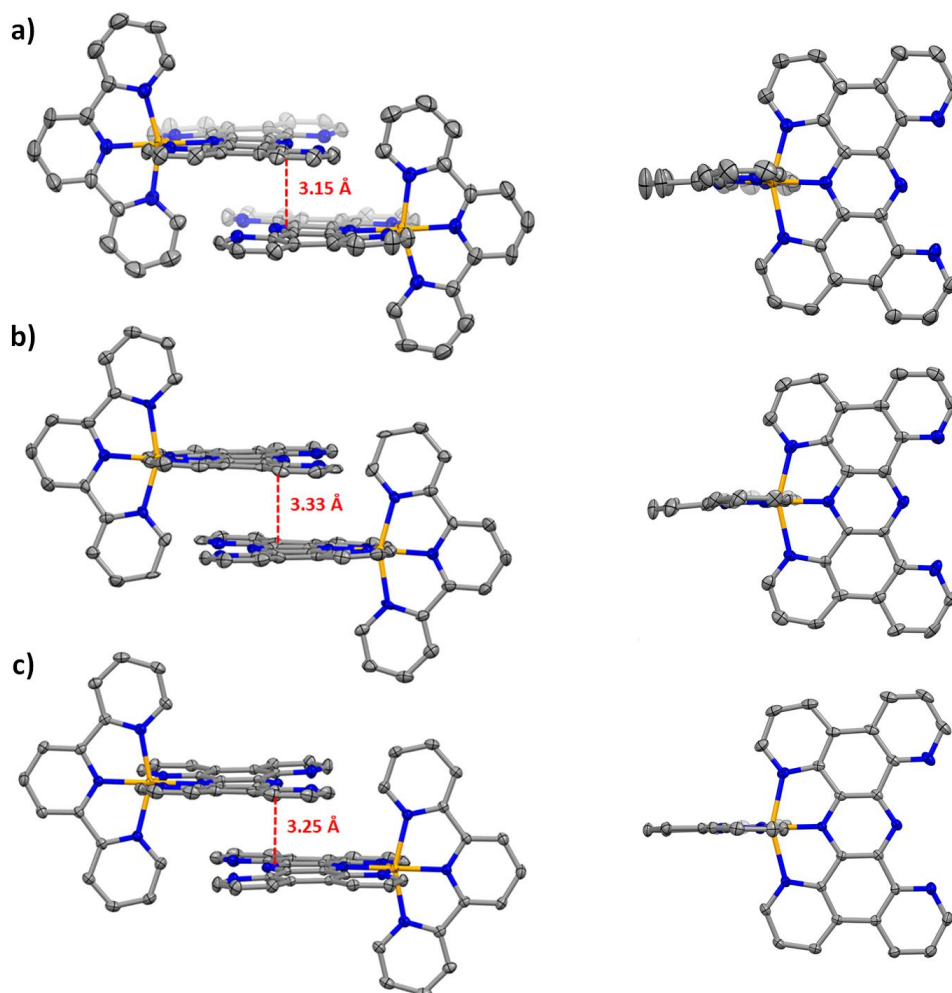


Figure S2. Two perpendicular ORTEP-type views (left and right) of the cationic complexes in **1** (a), **1^{red}** (b) and **1^{redred}** (c) at 120 K. The left part of the figure emphasizes their dimerization by π - π interactions with interplan distances. Orange: Cr; grey: C, blue: N. Thermal ellipsoids are depicted at a 50 % probability level. Hydrogen atoms are omitted for clarity.

Table S1. Crystal data and structure refinements.

Compound	Cr(tpy)(CF ₃ SO ₃) ₃	[Cr ^{III} (tphz)(tpy)](CF ₃ SO ₃) ₃ •Et ₂ O (1)	[Cr ^{III} (tphz ⁺)(tpy)](CF ₃ SO ₃) ₂ •CH ₃ CN (1 ^{red})	[Cr ^{III} (tphz ⁺)(tpy ⁻) ₂](CF ₃ SO ₃) ₂ •3CH ₃ CN•2Et ₂ O (1 ^{redred})
Formula	C ₁₈ H ₁₁ CrF ₉ N ₃ O ₉ S ₃	C ₄₆ H ₃₃ CrF ₉ N ₉ O ₁₀ S ₃	C ₄₃ H ₂₆ CrF ₆ N ₁₀ O ₆ S ₂	C ₉₄ H ₇₅ Cr ₂ F ₆ N ₂₁ O ₈ S ₂
FW (g·mol⁻¹)	732.48	1190.99	1008.86	1908.87
Crystal color	red	orange	brown	black
Crystal size (mm)	0.14×0.11×0.03	0.30×0.02×0.01	0.3×0.08×0.01	0.3×0.2×0.1
Crystal system	triclinic	triclinic	triclinic	triclinic
Space group	<i>P</i> -1	<i>P</i> -1	<i>P</i> -1	<i>P</i> -1
Temperature (K)	120	120	120	120
<i>a</i> (Å)	13.3872(15)	10.6856(11)	9.863(3)	10.8374(5)
<i>b</i> (Å)	13.4166(16)	13.1212(12)	12.837(3)	13.4385(6)
<i>c</i> (Å)	15.6840(18)	18.0622(18)	16.566(6)	15.1456(8)
<i>α</i> (°)	81.472(6)	72.344(4)	98.506(13)	81.115(2)
<i>β</i> (°)	68.974(5)	83.075(4)	100.189(12)	87.233(2)
<i>γ</i> (°)	85.355(6)	86.981(4)	98.847(12)	76.720(2)
<i>V</i> (Å³)	2599.2(5)	2395.2(4)	2006.4(11)	2120.85(18)
<i>Z</i>	4	2	2	1
<i>μ</i> (mm⁻¹)	0.801	0.475	0.484	0.393
<i>θ</i>_{min} - <i>θ</i>_{max}	1.535°-26.515°	1.190°-23.339°	1.632°-23.631°	1.573°-26.075°
Refl. coll. / unique	75346 / 10603	134816 / 6907	21534 / 5744	100958 / 8358
Completeness to 2θ	98.2	99.7	95.3	99.4
<i>R</i>_{int}	0.1043	0.1072	0.1500	0.025
Refined	775 / 0	703 / 71	614/0	604/0
Goodness-of-fit	1.020	1.059	1.029	1.109
^a<i>R</i>₁ (<i>I</i> > 2σ(<i>I</i>))	0.0455	0.1036	0.0736	0.0334
^b<i>wR</i>₂ (all data)	0.1188	0.3183	0.1997	0.0969
CCDC number	1954799	1954800	1954801	1954802

^a*R*₁ = $\sum||F_0| - |F_c|| / \sum|F_0|$ and ^b*wR*₂ = $[\sum w(F_0^2 - F_c^2)^2 / \sum w(F_0^2)^2]^{1/2}$

3. Spectroscopy data

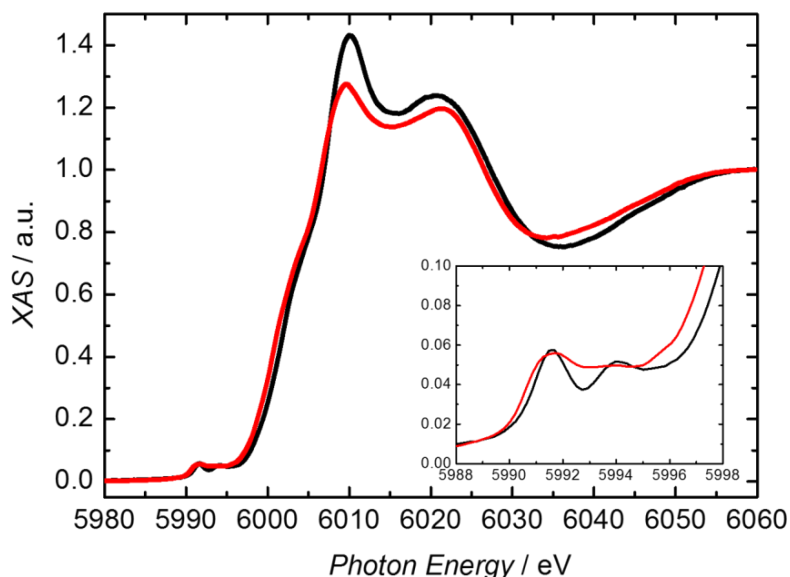


Figure S3. X-ray absorption spectroscopy (XAS) at Cr K-edge region for **1** (black) and **1^{red}** (red) at 295 K. To facilitate a direct comparison, recorded XAS spectra were normalized to zero before the edge and to unity far above the edge. Inset: magnification of the Cr K pre-edge region.

Comments: The local electronic properties of the chromium metal ions were studied by XAS to confirm the oxidation state assignments. These XAS spectra at the Cr K-edge are dominated by the $1s \rightarrow 4p$ transitions, which show similar maxima for the two complexes between 6006 and 6026 eV, with a good overlap of the first EXAFS (Extended X-ray Absorption Fine Structure) oscillations as expected for comparable coordination sphere. Two weaker pre-edge transitions are detected at 5991.6 ± 0.2 eV and 5994.1 ± 0.2 eV. The first absorption correspond to a dipole-forbidden $1s \rightarrow 3d$ transitions, for which the value is clearly consistent with a +3 oxidation state (comparable to the 5990.4 ± 0.4 and 5991.1 ± 0.2 eV reported for the Cr(III) ion in $\text{Cr}^{\text{III}}(\text{tpy})_2^{n+}$ with $n = 3, 2, 1$ or $[\text{Cr}^{\text{III}}\text{Cl}_2(\text{pyridine})_4](\text{ClO}_4) \cdot \frac{1}{4}\text{H}_2\text{O}$, and significantly higher in energy than the values obtained for Cr(II) ions).^[12-14] The second pre-edge absorption band at 5994.1 ± 0.2 eV is ascribed as a $1s \rightarrow \pi^*(\text{tpy})$ transition, with the exact same value obtained for $\text{Cr}^{\text{III}}(\text{tpy})_3^+$.^[12] In conclusion, these XAS spectra unambiguously demonstrate the same +3 oxidation state for the chromium centres in **1** and **1^{red}**.

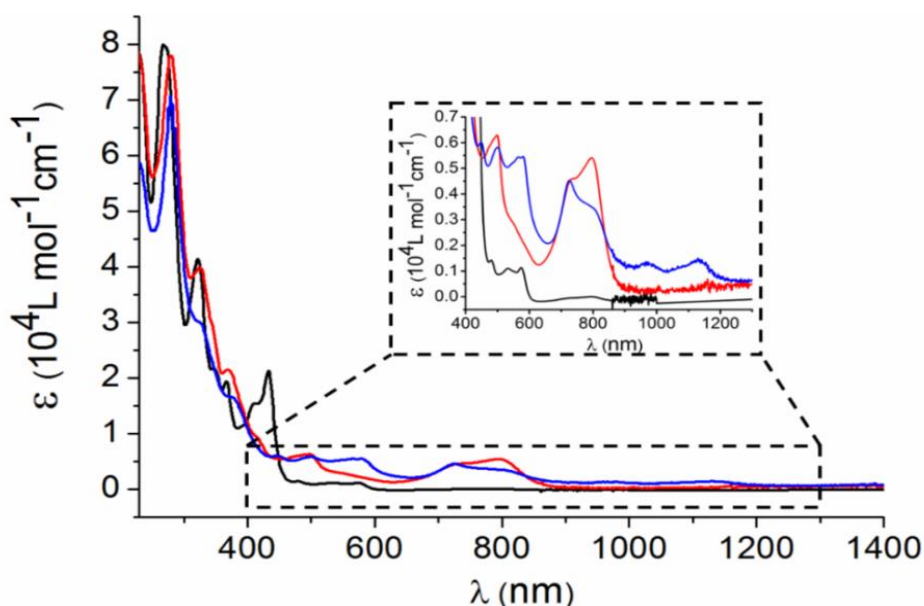


Figure S4. UV/visible/NIR spectra of **1** (black), **1^{red}** (red) and **1^{redred}** (blue) in CH₃CN at 298 K.

Comments: The absorption bands are assigned based on the reported spectra of comparable complexes like Cr(tpy)₂ⁿ⁺ (n = 1, 2, 3) and the dinuclear M₂(tphz)₂(tpy)₂ⁿ⁺ systems (M = Co and Ni, n = 2, 3, 4).^[12,15-19] For **1**, electronic transitions at 267, 323, 348 and 367 nm can be attributed to $\pi \rightarrow \pi^*$ transition of the ligands; and those at 408, 434, 480 and 532 nm can be assigned to ligand to metal charge transfer (LMCT), with similar values than those reported in Cr(tpy)₂³⁺, [Cr(ddpd)(tpy)]³⁺ (ddpd = N,N'-dimethyl-N,N''-dipyridin-2-yl-pyridine-2,6-diamine) and [Cr(ddpd)(tpy-COOEt)]³⁺ complexes in CH₃CN (between 200-400 nm for $\pi \rightarrow \pi^*$ and 400-550 nm for LMCT).^[15] An additional absorption band at 576 nm is due to metal to ligand charge transfer (MLCT). The above ascribed transitions are also observed in the spectra of **1^{red}** and **1^{redred}**. Besides, the band at 724 nm for **1^{red}** and 801 nm for **1^{redred}** indicate the π -acceptor character of the tphz ligand upon successive reductions, as observed in similar Co complexes.^[18] In **1^{redred}**, the weaker signals in the NIR region at 973 and 1132 nm are comparable to the electronic transitions reported for [Cr^{III}(tpy⁻)(tpy⁰)]²⁺ (905, 1000 nm), [Cr^{III}(tpy⁻)₂]⁺ (883, 1120 nm) and Li(tpy⁻) (950 nm),^[12,20] supporting the presence of the terpyridine radicals.

4. Electrochemistry

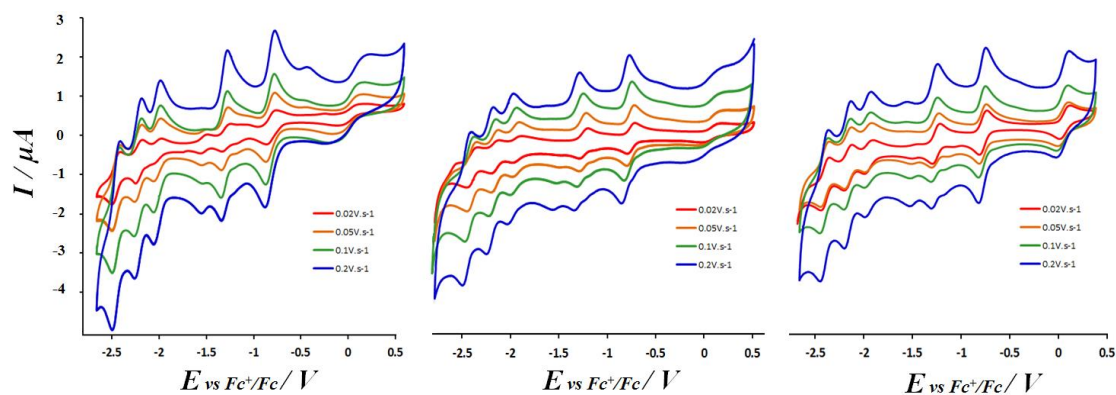


Figure S5. Cyclic voltammograms for a solution of **1** (left), **1^{red}** (middle) and **1^{redred}** (right) in CH₃CN at different scan rates; 0.1 M (*n*-Bu₄N)PF₆ as supporting electrolyte.

Comments: The results from the data at different scan rates indicate that all signals are diffusion dependent according to the proportionality of the intensity with the square root of the scan rate. As expected, the CV of **1**, **1^{red}** and **1^{redred}** were found to be exactly the same but with different rest potential (0.3, -0.1 and -0.8 V respectively), confirming that the reduction processes involve systematically one electron. An additional weaker signal at ca. -1.5 V is revealed at faster scan rate (Figures 2 & S5). Its systematic presence in all three samples indicates that this redox process is inherent to the complex, and could be explained by a kinetically controlled chemical reaction nearby the electrodes.

5. Computational details

a. Ab initio ligand field analysis.

The ligand field was computed with SOC-CASSCF(3,5)/def2-TZVP method, where 10 quartet and 40 doublet states were mapped onto crystal field Hamiltonian as implemented in ORCA 4.1.^[3] The charge of the reduced compounds was kept +3 to ensure that all unpaired electrons are localized on Cr(III). Local D- and g-tensors were computed in the similar fashion.

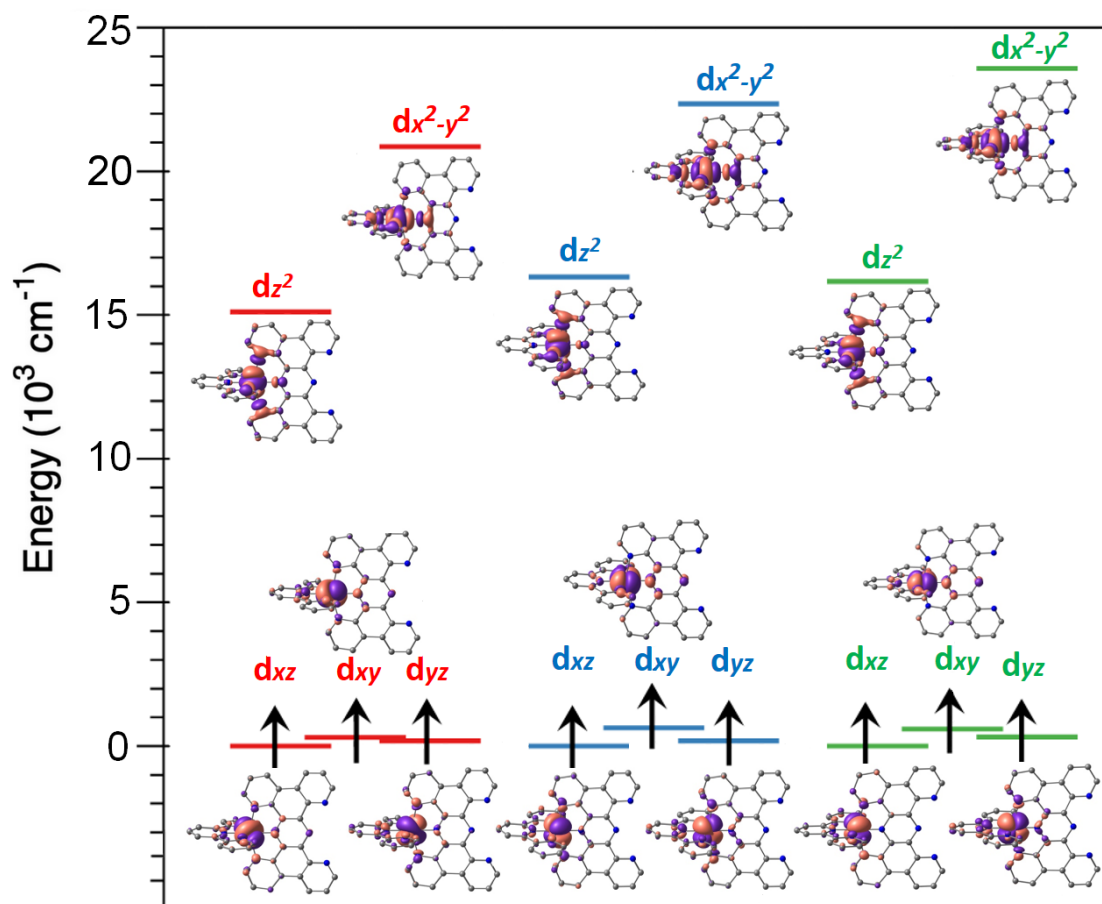


Figure S6. Ab initio ligand field analysis of Cr(III) 3d-orbitals based on CASSCF/NEVPT2 calculations of 10 quartet and 40 doublet states for XRD structures of **1** – red, **1^{red}** – blue, **1^{redred}** – green. Contour plots (0.03 iso-value) represent the ligand field orbitals, which are labeled by the leading atomic orbital contribution. Note that only unpaired electrons in d-shell were considered here.

Comments: The t_{2g} orbitals are very close in energy and each orbital is singly occupied, whereas e_g orbitals are much higher in energy, making the magnetic anisotropy of the complex very small. Unlike Ni and Co complexes, reduction of **1** does not lead to a significant splitting of t_{2g} orbitals, however there is a small increase in splitting between barycenter of t_{2g} and e_g orbital energies upon reduction that has only a minor effect on magnetic properties. This splitting of d -orbitals is characteristic for an elongated octahedron with a large splitting of e_g orbitals and the d_{z^2} orbital that is lower in energy than the $d_{x^2-y^2}$ orbital due to the bond lengths to the axial tpnz nitrogen atoms (Cr-N1 and Cr-N3; the average N1-Cr-N3 axis is taken as the z direction by convention) that are larger than the equatorial and other bond lengths (Cr-N_{*i*}; $i = 2, 7, 8, 9$, see Figure 1 and Table 1).

b. Intramolecular exchange interaction from broken-symmetry approach.

The exchange interactions have been computed using the broken-symmetry approach as implemented in ORCA 4.1^[3] with B3LYP/def-TZVP method on experimental X-ray crystal structures. In the case of two spin centers, the broken-symmetry solution is an open-shell low-spin state, which corresponds to a spin flip on one of the two sites. In the present cases, the Cr(III) metal ion is assumed to possess a quartet state. The exchange coupling constant (J) of once reduced complex is computed as:^[21]

$$J = -\frac{E_{HS} - E_{BS}}{\langle S^2 \rangle_{HS} - \langle S^2 \rangle_{BS}}$$

with E_{HS} and $\langle S^2 \rangle_{HS}$ being the energy and the expectation value of the squared spin operator of the maximum multiplicity state, E_{BS} is the energy of the open-shell low-spin and $\langle S^2 \rangle_{BS}$ its expectation value. In the case of a three spin system like tpy⁻-Cr(III)-tphz⁻, there are four broken-symmetry solutions: “DUU” – where the spin is flipped on tpy⁻ fragment, “UDU” – where the Cr(III) spin is flipped, and “UUD” - where the tphz⁻ spin is flipped. However, both states DUU and UUD have very similar energy and expectation values, suggesting that exchange interactions between metal and radical are very similar $J_{Cr-tpy^-} = J_{Cr-tphz^-} = J_{Cr-Rad}$. Therefore, two exchange unique interactions can be computed using the Heisenberg Hamiltonian:

$$J_{Cr-R} = -\frac{E_{UUU} - E_{UDU}}{\langle S^2 \rangle_{UUU} - \langle S^2 \rangle_{UDU}}$$

$$J_{R-R} = -\frac{\frac{1}{2}(E_{UUU} + E_{UDU}) - \frac{1}{2}(E_{DUU} + E_{UUD})}{\frac{3}{4}\langle S^2 \rangle_{UUU} + \frac{1}{4}\langle S^2 \rangle_{UDU} - \frac{1}{2}(\langle S^2 \rangle_{UUD} + \langle S^2 \rangle_{DUU})}$$

Without the assumption of such symmetry, Heisenberg Hamiltonian cannot be used, instead Ising model can be applied to extract all three exchange parameters.

Table S2. Local spin Hamiltonian parameters computed with SOC-CASSCF(3,5)/NEVPT2

	$D/hc, \text{cm}^{-1}$	E/D	g_1	g_2	g_3
1	-0.290132	0.324956	1.969782	1.974491	1.978145
1^{red}	-0.202503	0.234864	1.971364	1.977886	1.978917
1^{redred}	-0.214853	0.190054	1.971154	1.977679	1.980158

	g^{iso}_{Cr}	$J_{Cr-tphz^-}/hc (\text{cm}^{-1})$	$J_{Cr-tpy^-}/hc (\text{cm}^{-1})$	$J_{tphz^-tphz^-}/hc (\text{cm}^{-1})$
1	1.97	-	-	-
1^{red}	1.98	-1303	-	-19
1^{redred}	1.98	-1223*	-1172*	-33

*Ising Hamiltonian was used

b.1. [Cr(tphz)(tpy)]³⁺ complex in 1.

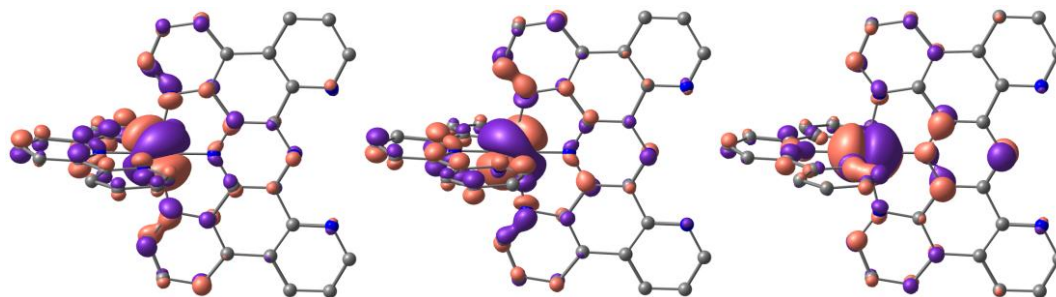


Figure S7. SOMOs of [Cr(tphz)(tpy)]³⁺ in **1** showing the unpaired electrons mainly localized in the d_{yz} , d_{xz} and d_{xy} orbitals of the Cr site.

b.2. Once reduced complex, [Cr^{III}(tphz⁻)(tpy)]²⁺, in **1^{red}.**

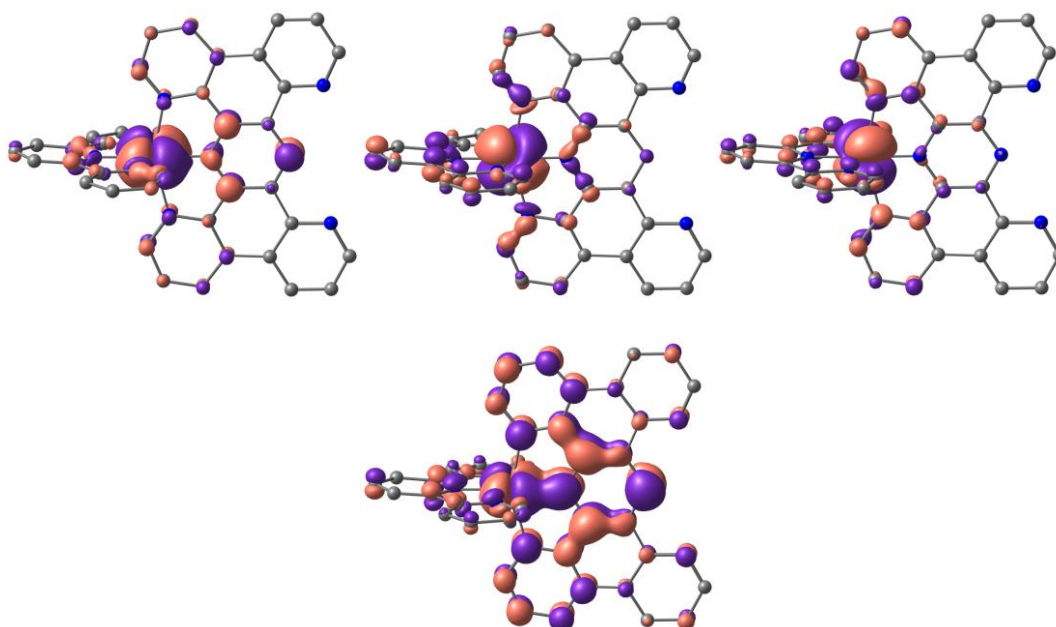


Figure S8. SOMOs of [Cr^{III}(tphz⁻)(tpy)]²⁺ in **1^{red}**.

b.3. Twice reduced complex, [Cr^{III}(tphz⁻)(tpy⁻)]⁺, in **1^{redred}.**

Table S3. Computed energies and corresponding S^2 expectation values for the different broken-symmetry configurations.

Configuration	E (a.u.)	$\langle S^2 \rangle$
UUU	-3037.615264	8.7865
UUD	-3037.631381	4.4830
UDU	-3037.648008	2.1498
DUU	-3037.632081	4.4459

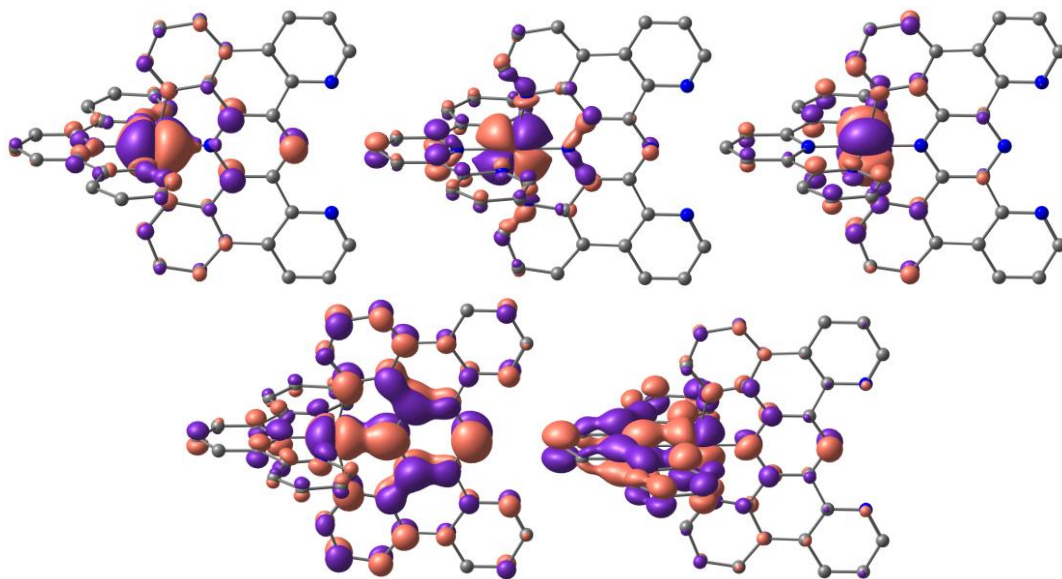


Figure S9. SOMOs of [Cr^{III}(tphz⁻)(tpy⁻)]⁺ in **1^{redred}**.

6. Additional magnetic data

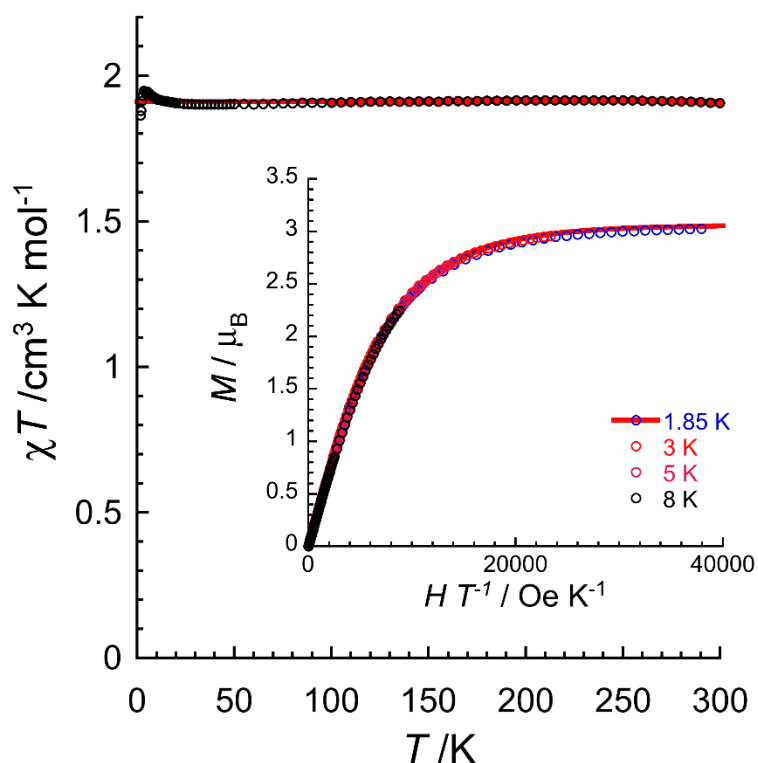


Figure S10. Temperature dependence of the χT product for **1** at 0.1 T between 1.85 and 40 K and at 1 T above 40 K (χ is defined as magnetic susceptibility equal to M/H per mole of complex). Inset: magnetization (M) versus field (H) curves plotted as M vs H/T for **1** below 8 K. The solid red lines represent the best fits of the experimental data considering a magnetically isolated $S = 3/2$ Cr^{III} spins. Hence, a Curie law with $C = 1.91(5) \text{ cm}^3 \text{ K mol}^{-1}$ (and thus $g = 2.02(4)$; main part) has been used to reproduce the χT vs T data down to 30 K, while a $S = 3/2$ Brillouin function with $g = 2.04(2)$ (inset) was considered for the M vs H/T data below 8 K. Please note that the increase of the χT product between 30 and 4.5 K is certainly the sign of weak intermolecular ferromagnetic interactions, while its decrease below 4.5 K indicates the presence of local magnetic anisotropy induced by the distortion of the $\text{Cr}(\text{III})$ coordination sphere (see Table S2). With our available data down to 1.8 K and due to the weak amplitude of these effects, it was not possible to simulate the experimental data including with these two contributions.

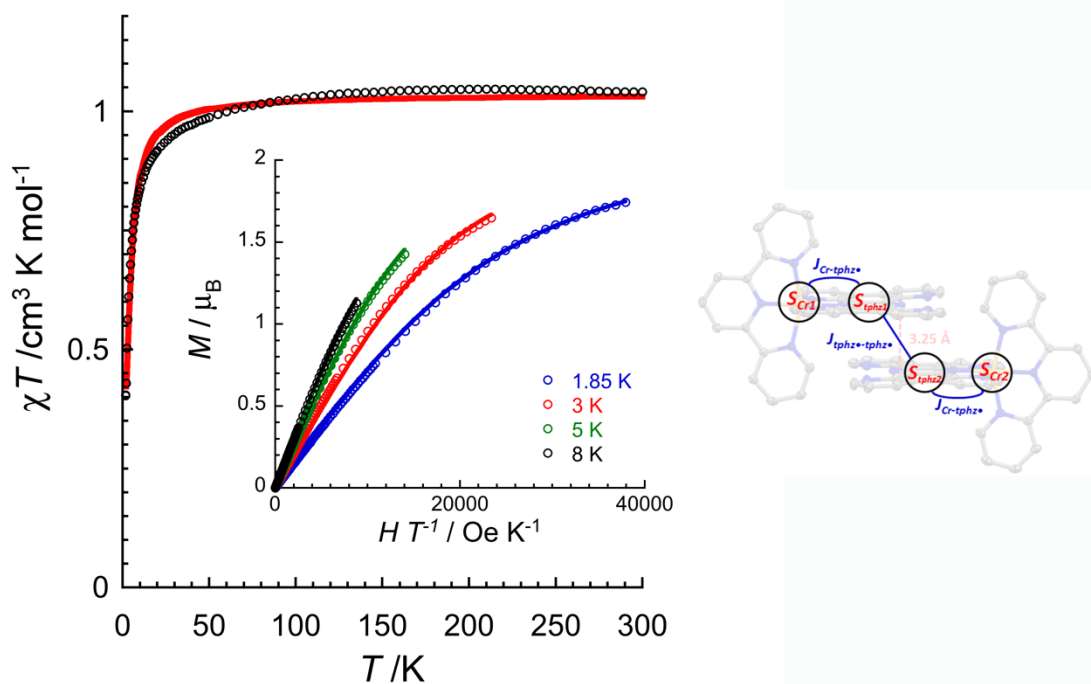


Figure S11. Temperature dependence of the χT product for **1^{red}** at 0.1 T between 1.85 and 40 K and at 1 T above 40 K (χ is defined as magnetic susceptibility equal to M/H per mole of complex). Inset: magnetization (M) versus field (H) curves plotted as M vs H/T for **1^{red}** below 8 K. The solid lines represent the best fit of the experimental data considering a pair of complexes as discussed in the comment below and illustrated by the four-spins model on the right part of the figure.

Comments: A four-spins model (see scheme above) with the following Heisenberg spin Hamiltonian was first considered to fit the above magnetic data with the PHI software:^[22]

$$\hat{H} = -2J_{tpbz\bullet-tpbz\bullet}(\vec{S}_{tpbz\bullet 1} \cdot \vec{S}_{tpbz\bullet 2}) - 2J_{Cr-tpbz\bullet}(\vec{S}_{Cr1} \cdot \vec{S}_{tpbz\bullet 1} + \vec{S}_{Cr2} \cdot \vec{S}_{tpbz\bullet 2}) + 2D_{Cr}S_{Cr,z}^2$$

Staying below 300 K, for which the complex is stable, the susceptibility measurements take place in the limit where $J_{Cr-tpbz\bullet} \gg k_B T$, and thus this interaction cannot be experimentally determined. Therefore, in order to ensure the $S_T = 1$ ground state to be thermally isolated from the excited states in the fitting process, $J_{Cr-tpbz\bullet}$ was fixed at -1000 K. As expected in this case, the χT product is constant below 300 K until intermolecular $J_{tpbz\bullet-tpbz\bullet}$ interactions or the local Cr^{III} magnetic anisotropy become of the order of $k_B T$. A reasonable fit of both χT vs. T and M vs. H/T curves (shown in Figure S11) was achieved with $g_{tpbz\bullet}$ fixed at 2, and $D_{Cr}/k_B = +5.7(3)$ K, $g_{Cr} = 2.03(5)$ and $J_{tpbz\bullet-tpbz\bullet}/k_B = -16.5(4)$ K as the final optimized parameters. It is worth noting that the estimation of the coupling obtained by DFT (-27 K) is comparable to the one experimentally determined.

An alternative model was used considering the complex **1^{red}** as a $S_T = 1$ macrospin as it is indeed the case at room temperature due to the massive $J_{Cr-tpbz\bullet}$ coupling. In this approach, the following simplified Heisenberg spin Hamiltonian was used, considering the effective coupling,

J , between the two paired $S_T = 1$ macrospins (see scheme above) and their magnetic anisotropy, D :

$$\hat{H} = -2J\vec{S}_T \cdot \vec{S}_T + 2DS_{T,z}^2$$

This model is completely equivalent to the first one and give virtually identical fits of the experimental data with $g = 2.02(5)$, $D/k_B = +6.1(3)$ K and $J/k_B = -0.71(4)$ K.

However, the obtained values of D and the intermolecular exchanges, J or $J_{\text{tphz}^*-\text{tphz}^*}$, must be taken with care from both models as both effects are small and lead to similar effects at low temperature on the magnetic data. In addition, it was found that the sign of the magnetic anisotropy D/k_B has only a minor influence on the fitting result.

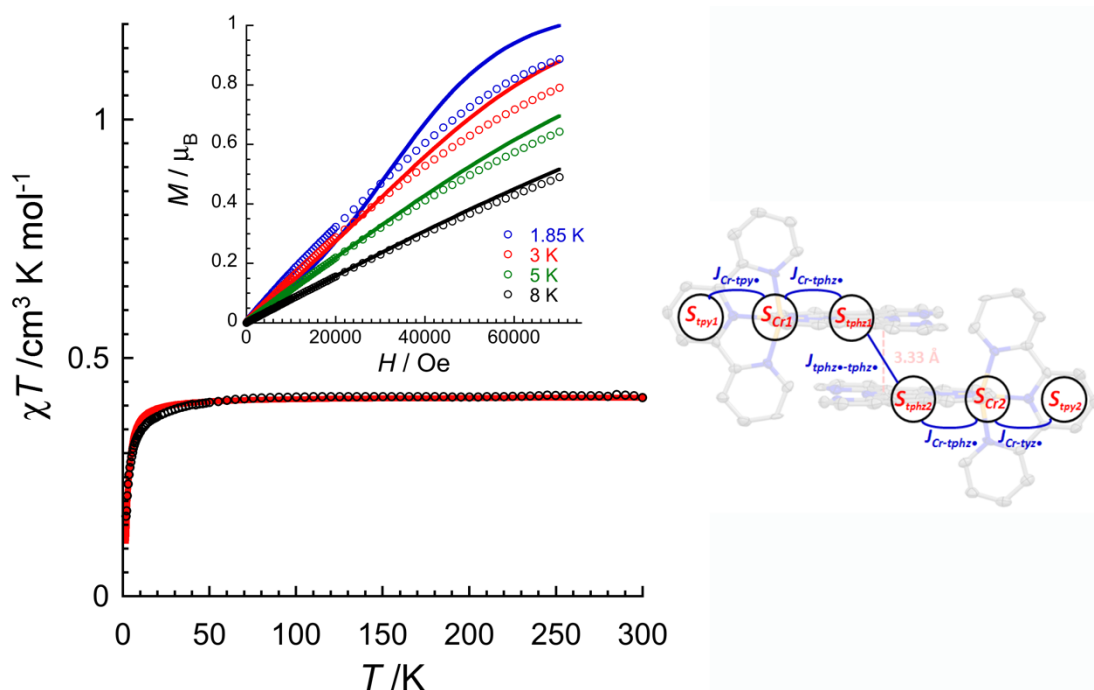


Figure S12. Temperature dependence of the χT product for **1^{redred}** at 0.1 T between 1.85 and 40 K and at 1 T above 40 K (χ is defined as magnetic susceptibility equal to M/H per mole of complex). Inset: magnetization (M) versus field (H) curves for **1^{redred}** below 8 K. The solid lines represent the best fit of the experimental data considering a pair of complexes as discussed in the comment below and illustrated by the six-spins model on the right part of the figure.

Comments: A six-spins model (see scheme above) with the following Heisenberg spin Hamiltonian was first considered to fit the above magnetic data with the PHI software:^[22]

$$\hat{H} = -2J_{tphz^*-tphz^*}(\vec{S}_{tphz1} \cdot \vec{S}_{tphz2}) - 2J_{Cr-rad}(\vec{S}_{Cr1} \cdot \vec{S}_{tpy1} + \vec{S}_{Cr1} \cdot \vec{S}_{tphz1} + \vec{S}_{Cr2} \cdot \vec{S}_{tphz2} + \vec{S}_{Cr2} \cdot \vec{S}_{tpy2})$$

Staying below 300 K, for which the complex is stable, the susceptibility measurements take place in the limit where $J_{Cr-tphz^*} \gg k_B T$ and $J_{Cr-tpy^*} \gg k_B T$, and thus these interactions cannot be experimentally determined. Therefore, in order to ensure the $S_T = 1/2$ ground state to be thermally isolated from the excited states in the fitting process, J_{Cr-Rad} were set to be equal as suggested by the DFT calculation and fixed at -1000 K. As expected in this case, the χT product is constant below 300 K until intermolecular $J_{tphz^*-tphz^*}$ interactions become of the order of $k_B T$. A reasonable fit of both χT vs. T and M vs. H/T curves (shown in Figure S12) was achieved with g_{tphz^*} and g_{tpy^*} fixed at 2, $g_{Cr} = 2.07(5)$ and $J_{tphz^*-tphz^*}/k_B = -20.2(5)$ K as the final optimized parameters. It is worth noting that the estimation of the coupling obtained by DFT (-47 K) is comparable to the one experimentally determined and that the addition of a magnetic anisotropy term (D/k_B) for Cr(III) ions do not improve the fitting result and thus leads to overparametrization.

An alternative model was used considering the complex **1^{redred}** as a $S_T = 1/2$ macrospin as it is indeed the case at room temperature due to the massive $J_{Cr-tphz^*}$ and J_{Cr-tpy^*} couplings. In this approach, the following simplified Heisenberg spin Hamiltonian was used, considering the effective coupling, J , between the two paired $S_T = 1/2$ macrospins (see scheme above):

$$\hat{H} = -2J\vec{S}_T \cdot \vec{S}_T$$

This model is completely equivalent to the first one and give virtually identical fits of the experimental data with $g = 2.13(5)$ and $J/k_B = -2.3(2)$ K.

However, the obtained values of the intermolecular exchanges, J or $J_{tphz^*-tphz^*}$, must be taken with care from both models as the quality of the fits is not optimum. It is clear that additional weak effects are present in this compound like the local Cr^{III} magnetic anisotropy but the models including this additional effect were not able to improve the fits and to reproduce the experimental data as well as for complex **1^{red}**.

7. References

- [1] G. M. Sheldrick, SADABS Version 2.03, Bruker Analytical X-Ray Systems, Madison, WI, USA, 2000.
- [2] G. M. Sheldrick, *Acta Cryst.* **2015**, C71, 3-8.
- [3] F. Neese, *WIREs Comput. Mol. Sci.* **2012**, 2, 73-78.
- [4] M. Atanasov, D. Ganyushin, K. Sivalingam, F. Neese, *A Modern First-Principles View on Ligand Field Theory Through the Eyes of Correlated Multireference Wavefunctions*. In: D. Mingos, P. Day, J. Dahl (eds) *Molecular Electronic Structures of Transition Metal Complexes II. Structure and Bonding*, **2011**, 143. Springer, Berlin, Heidelberg.
- [5] D. Ganyushin, F. Neese, *J. Chem. Phys.*, **2013**, 138, 104113.
- [6] M. D. Hanwell, D. E. Curtis, D. C. Lonie, T. Vandermeersch, E. Zurek, G. R. Hutchison, *J. Chem. Phys.*, **2013**, 138, 104-113.
- [7] K. Nakayama, Z. Sogo, H. Cai, T. Yasuda, T. Shiono, *Polym. Int.* **2011**, 60, 692-697.
- [8] E. C. Constable, C. E. Housecroft, M. Neuburger, J. Schönle, J. A. Zampese, *Dalton Trans.* **2014**, 43, 7227-7235.
- [9] P. Bonhôte, A. Lecas, E. Amouyal, *Chem. Commun.* **1998**, 8, 885-886.
- [10] P. Bonhôte, M. S. Wrighton, *Synlett.* **1997**, 897-898.
- [11] D. M. D'Alessandro, F. R. Keene, *Dalton Trans.* **2006**, 8, 1060-1072.
- [12] C. C. Scarborough, K. M. Lancaster, S. DeBeer, T. Weyhermüller, S. Sproules, K. Wieghardt, *Inorg. Chem.* **2012**, 51, 3718-3732.
- [13] C. C. Scarborough, S. Sproules, C. J. Doonan, K. S. Hagen, T. Weyhermüller, K. Wieghardt, *Inorg. Chem.* **2012**, 51, 6969-6982.
- [14] K. S. Pedersen, P. Perlepe, M. L. Aubrey, D. N. Woodruff, S. E. Reyes-Lillo, A. Reinholdt, L. Voigt, Z. Li, K. Borup, M. Rouzières, D. Samohvalov, F. Wilhelm, A. Rogalev, J. B. Neaton, J. R. Long, R. Clérac, *Nature Chem.* **2018**, 10, 1056-1061.
- [15] J.-R. Jiménez, B. Doistau, C. Besnard, C. Piguet, *Chem. Commun.* **2018**, 54, 13228-13231.
- [16] N. Serpone, M. Jamieson, M. Henry, M. Hoffman, F. Bolletta, M. Maestri, *J. Am. Chem. Soc.* **1979**, 101, 2907-2916.
- [17] T. Ohno, S. Kato, S. Kaizaki, I. Hanazaki, *Inorg. Chem.* **1986**, 25, 3853-3858.
- [18] X. Ma, E. A. Suturina, S. De, P. Négrier, M. Rouzières, R. Clérac, P. Dechambenoit, *Angew. Chem. Int. Ed.* **2018**, 57, 7841-7845.
- [19] X. Ma, E. A. Suturina, S. De, M. Rouzières, R. Clérac, P. Dechambenoit, *J. Am. Chem. Soc.* **2019**, 141, 19, 7721-7725.
- [20] P. S. Braterman, J. L. Song, R. D. Peacock, *Inorg. Chem.* **1992**, 31, 555-559.
- [21] (a) K. Yamaguchi, Y. Takahara, T. Fueno in *Applied Quantum Chemistry*. V. H. Smith (Ed.), Reidel, Dordrecht (1986), pp 155; (b) T. Soda, Y. Kitagawa, T. Onishi, Y. Takano, Y. Shigeta, H. Nagao, Y. Yoshioka, K. Yamaguchi. *Chem. Phys. Lett.*, **2000**, 319, 223-230.
- [22] N. F. Chilton, R. P. Anderson, L. D. Turner, A. Soncini, J. S. Murray, *J. Comput. Chem.* **2013**, 34, 1164-1175.